buildings

MDPI

Article

Two-Stage Distributionally Robust Optimization for Intelligent Buildings Integrating Virtual Energy Storage

Haibo Yang [1,*], Yifan Lv [2] and Song Zhang [2]

[1] School of Energy and Architectural Engineering, Shandong Huayu University of Technology, Dezhou 253000, China
[2] School of Electrical Engineering, Northeast Electric Power University, Jilin 132012, China
* Correspondence: p20232002880@siswa.upsi.edu.my

Abstract

To improve the sustainability of intelligent building operation and enhance grid adaptability in the presence of uncertainty, this paper presents a coordinated optimization method that jointly exploits virtual energy storage and waste heat recovery. A thermal modeling framework is developed to represent the coupling relationships among air conditioning operation, waste heat utilization, and indoor comfort requirements. On this basis, building thermal inertia is incorporated into an IDM-informed two-stage robust optimization framework, where distributional bounds derived from the Imprecise Dirichlet Model are transformed into data-driven interval uncertainty sets for wind–photovoltaic output and outdoor temperature. To make the model computationally tractable, the column-and-constraint generation method is employed for iterative solution. Numerical results verify that the proposed method can effectively unlock the flexibility of the cooling system and improve the utilization of recoverable heat resources while maintaining acceptable indoor comfort, even under adverse operating conditions. Overall, the proposed strategy strengthens system resilience, reduces carbon-related operational pressure, and provides more dependable demand-side support for secure power system operation.

Keywords: low-carbon intelligent buildings; distributionally robust optimization; virtual energy storage; waste heat recovery; resilience-oriented optimization

1. Introduction

With the ongoing acceleration of urbanization in China, building-related energy demand has continued to increase year by year [1]. As a typical type of high-energy-consuming facility, intelligent buildings are now facing increasing pressure to enhance energy efficiency and move toward low-carbon operation [2]. From a global perspective, the building sector accounts for a substantial proportion of overall energy use, approaching one-third of total consumption, and the energy demand of commercial and office-based intelligent buildings is still growing steadily [3,4]. Within these buildings, major end-use systems such as air conditioning equipment and information technology devices consume a dominant share of electricity, together contributing to more than half of the total energy demand. Owing to their large consumption and high operational intensity, these systems have become crucial targets in efforts to reduce building carbon emissions and improve overall energy performance [5].

Building envelopes generally exhibit considerable thermal inertia and heat buffering capacity, which enable thermal storage and peak-shifting functions and thereby endow

Check for updates

Academic Editor: Francesco Nocera

Received: 31 March 2026
Revised: 1 June 2026
Accepted: 10 June 2026
Published: 13 June 2026

Copyright: © 2026 by the authors. Licensee MDPI, Basel, Switzerland. This article is an open access article distributed under the terms and conditions of the Creative Commons Attribution (CC BY) license.

buildings with inherent operational flexibility and virtual energy storage capability [6,7]. This characteristic becomes especially important when internal loads or outdoor conditions vary rapidly, as the thermal dynamic behavior of the building envelope can help buffer cooling demand fluctuations and enhance operational stability [8]. Moreover, intelligent buildings contain several forms of recoverable waste heat, such as exhaust air, waste hot water, and heat released by equipment during operation. Existing studies have demonstrated that improving the recovery and reuse of these internal heat sources is an effective approach to enhancing overall energy efficiency and lowering carbon emissions [9,10]. Accordingly, the coordinated use of building thermal inertia and internal waste heat recovery offers significant potential for promoting flexible, efficient, and low-carbon operation in intelligent buildings. Recovered heat can be reused for space heating and hot water supply, thereby reducing the overall cooling and heating demand. Meanwhile, the joint deployment of virtual energy storage and waste heat recovery can decrease electricity and maintenance costs, improve indoor air quality and thermal comfort, and ultimately enhance user experience. As an economical and low-carbon solution, building-level waste heat recovery therefore plays an important role in advancing net-zero energy buildings and carbon neutrality goals.

However, the operation of intelligent buildings is highly susceptible to uncertainties associated with varying load demand and external weather conditions, especially fluctuations in outdoor temperature, which pose significant difficulties for the coordinated management of air conditioning and energy systems [11,12]. These uncertainties can lead to mismatches between scheduled plans and actual operating states, thereby making it more challenging to simultaneously guarantee occupant comfort, system efficiency, and economic performance. At present, the optimization methods commonly adopted for this type of problem mainly include stochastic optimization and robust optimization [13,14]. The former depends on accurate probability distributions and usually requires large amounts of historical data, which limits its practical applicability. The latter, by contrast, relies on uncertainty sets and is more adaptable when precise distributional information is unavailable. However, conventional robust optimization methods typically employ fixed uncertainty sets, which may lead to overly conservative scheduling decisions in integrated energy systems and consequently reduce operational flexibility while increasing costs under source-load uncertainty [15].

Recent studies have increasingly explored the flexibility potential of building thermal dynamics in broader resilience-oriented energy applications. For example, Li et al. [16] proposed an asynchronous decentralized restoration framework for electricity–transportation networks and demonstrated that the coordinated response of buildings and electric buses can substantially enhance post-disaster load recovery, thereby confirming the applicability of building thermal inertia in coupled multi-network systems. Likewise, other studies have shown that the coordinated reconfiguration of integrated electricity and heating networks can significantly improve multi-stage resilience and system planning performance [17,18]. In addition, the combination of virtual energy storage and waste heat recovery has shown considerable promise for enabling low-carbon operation in extreme environments. Chang et al. [19] developed a two-stage distributionally robust optimization model for an Antarctic unmanned observation station by integrating virtual energy storage with hydrogen waste heat recovery, achieving a significant reduction in carbon emissions and offering useful insights for intelligent building energy management. Lu et al. [20] proposed a data-driven two-stage distributionally robust optimization framework for multi-energy hubs and demonstrated that ambiguity sets constructed from data can effectively balance economy and robustness under energy price uncertainty. Although their work focuses on multi-energy hubs rather than buildings, the adopted DRO framework is highly relevant to intelligent building operation, where HVAC loads are also subject to considerable un-

certainty. Zhang et al. [21] introduced a distributionally robust configuration method for island microgrids using extreme scenarios generated by conditional generative adversarial networks to enhance renewable energy resilience. Their scenario construction strategy provides a useful reference for building-side flexibility modeling, especially when on-site photovoltaic and wind generation are incorporated under highly uncertain outputs. Zhang et al. [22] further developed a constrained DRO model for day-ahead dispatch of rural integrated energy systems, providing a flexible trade-off between expected cost and robustness through historical-data-based uncertainty sets. This idea is closely aligned with intelligent building operation, where thermal inertia, demand response capability, and occupant comfort must be jointly managed under uncertain environmental conditions.

To address these issues, particularly the challenge of achieving a balance between robustness and economic performance under uncertainty, as well as the overly conservative nature of existing methods, this study develops an IDM-informed two-stage robust optimization framework that incorporates virtual energy storage and waste heat recovery. The IDM is first used to characterize distributional uncertainty under limited data, and the resulting probability bounds are then mapped into physical interval uncertainty sets for wind–photovoltaic output and outdoor temperature. A spatiotemporal coordination model is further established to explicitly represent indoor thermal comfort requirements. By introducing adjustable uncertainty parameters, the proposed method allows the conservatism level of the optimization process to be flexibly tuned, thereby enabling a dynamic trade-off between system robustness and economic efficiency. The resulting problem is solved using a column-and-constraint generation (C&CG) algorithm. During the solution procedure, the master problem and subproblem are iteratively reconstructed and solved as mixed-integer linear programming models. The results show that the proposed approach can fully exploit the regulation capability of the air conditioning system as well as the reusable potential of waste heat resources. Even in adverse operating scenarios, it is still able to maintain indoor thermal comfort while ensuring stable, economical, and low-carbon operation of intelligent buildings.

The remainder of this paper is organized as follows: Section 2 presents the overall operating framework of the intelligent building system and explains the interactions among its major components. Section 3 establishes the optimization model, covering building thermal dynamics, occupant comfort requirements, and the mathematical models of the related energy subsystems. Section 4 describes the solution approach, with emphasis on the two-stage distributionally robust optimization method and the implementation of the C&CG algorithm. Section 5 provides and analyzes the simulation results under different uncertainty conditions and system configurations. Finally, Section 6 concludes the paper and discusses possible directions for future work.

2. Operational Framework for IBs

Figure 1 illustrates the proposed coordinated multi-source energy supply system for intelligent buildings (IBs), which consists primarily of local photovoltaic (PV) generation, wind turbines (WTs), the utility grid, an energy storage system (ESS), air conditioning (AC) loads, conventional electrical loads, and a waste heat recovery (WHR) unit. Through the coordinated interaction of these components, the system is able to support flexible, reliable, and efficient energy management for intelligent buildings. The electricity demand of IBs can be broadly divided into two main categories. The first category is conventional electrical load, which includes lighting systems, elevators, office equipment, and other routine building power demands. The second category is the AC load, which plays a critical role in maintaining indoor thermal comfort and therefore typically requires continuous or frequent operation. Compared with conventional loads, AC systems usually exhibit

stronger coupling with indoor thermal dynamics and provide greater flexibility for building energy management. Accordingly, the coordinated scheduling of these two types of loads is essential for improving the operational efficiency and low-carbon performance of intelligent buildings.

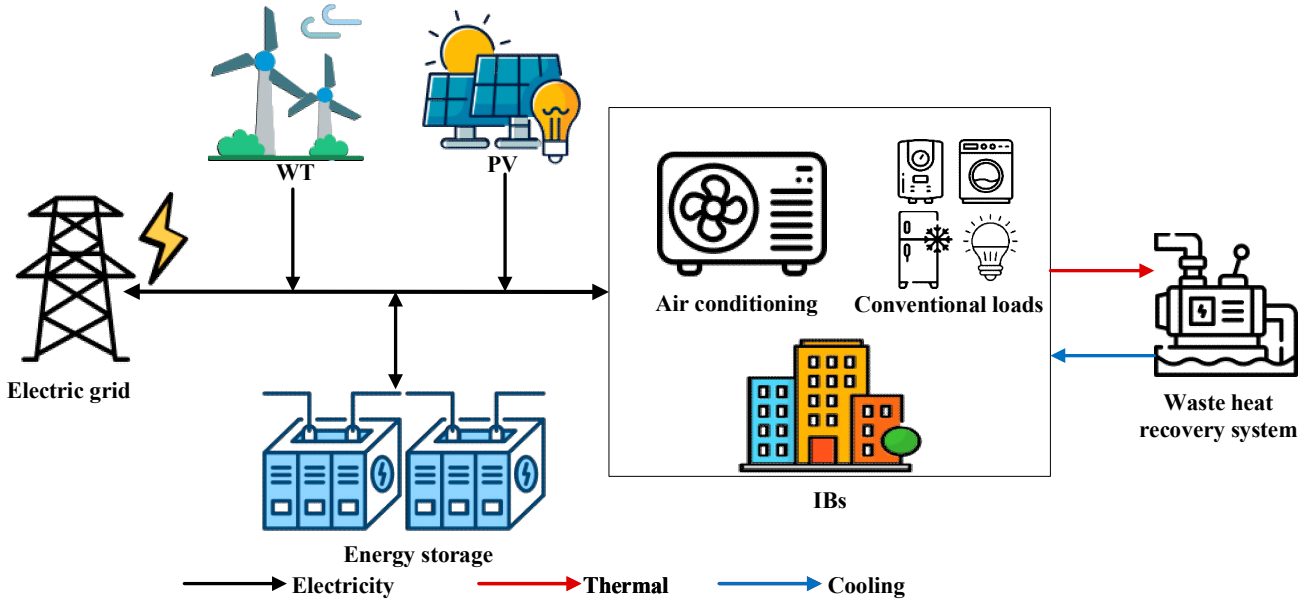

Figure 1. Operational framework for IBs.

Within this framework, local PV and WT generation can directly serve building loads, while bidirectional interaction with the utility grid is also allowed. Specifically, electricity can be purchased from the grid when local renewable output is insufficient, whereas surplus electricity can be exported during periods of excess generation. In this way, the system improves both operational flexibility and economic performance. In addition, the integrated WHR unit can effectively capture low-grade thermal energy generated during building operation. The recovered heat is then used to drive absorption chillers, thereby partially substituting the electricity demand of conventional vapor-compression air conditioning systems. Through this heat recovery and reutilization pathway, the electrical burden of the cooling system is reduced, and a multi-energy complementary mode combining cooling and power supply is realized.

3. IBs Optimization Model

3.1. IBs Thermal Dynamic Model

In this study, the thermal behavior of the building envelope is modeled using a resistor–capacitor (RC) network approach [23]. The RC network representation for a single building zone is illustrated in Figure 2. Within this framework, thermal resistance R is used to characterize the heat transfer between the envelope and the indoor air, whereas thermal capacitance C reflects the heat storage capacity of the building materials. To ensure indoor thermal comfort, the air conditioning system adjusts the heat flux so that the indoor temperature can be maintained within the prescribed comfort range.

The thermal balance constraint for the enclosure structure is formulated as follows:

$$C^{wall,12}\left(T^{wall,12}_{w,n,t+1} - T^{wall,12}_{w,n,t}\right) = \Delta t\left(\frac{T^{in}_{w,n,t} - T^{wall,12}_{w,n,t}}{R_{wall,12}} + \frac{T^{adj,12}_{w,n,t} - T^{wall,12}_{w,n,t}}{R_{wall,12}}\right) \quad (1)$$

$$C^{wall,13}\left(T^{wall,13}_{w,n,t+1} - T^{wall,13}_{w,n,t}\right) = \Delta t\left(\frac{T^{in}_{w,n,t} - T^{wall,13}_{w,n,t}}{R_{wall,13}} + \frac{T^{adj,13}_{w,n,t} - T^{wall,13}_{w,n,t}}{R_{wall,13}}\right)\frac{-b \pm \sqrt{b^2 - 4ac}}{2a} \tag{2}$$

$$C^{wall,14} \cdot \left(T^{wall,14}_{w,n,t+1} - T^{wall,14}_{w,n,t}\right) = \Delta t\left(\frac{T^{in}_{w,n,t} - T^{wall,14}_{w,n,t}}{R_{wall,14}} + \frac{T^{out}_{w,n,t} - T^{wall,14}_{w,n,t}}{R_{wall,14}}\right) + \Delta t q^{14} \nu^{14} A^{wall,14} Q^{rad,14}_{w,n,t} \tag{3}$$

$$C^{wall,15}\left(T^{wall,15}_{w,n,t+1} - T^{wall,15}_{w,n,t}\right) = \Delta t\left(\frac{T^{in}_{w,n,t} - T^{wall,15}_{w,n,t}}{R_{wall,15}} + \frac{T^{out}_{w,n,t} - T^{wall,15}_{w,n,t}}{R_{wall,15}}\right) + \Delta t q^{15} \nu^{15} A^{wall,15} Q^{rad,15}_{w,n,t} \tag{4}$$

$$C^{room,j}(T^{in}_{t+1} - T^{in}_{t}) = \Delta t\Big(\sum_{j \in N_{room}} \frac{T^{wall,1j}_{t} - T^{in}_{t}}{R^{wall,1j}_{t}} + \frac{T^{out}_{w,n,t} - T^{in}_{t}}{R^{win,15}_{t}} + \omega^{15} A^{win,15}_{t} Q^{rad,1}_{t} + Q^{\mathrm{int},j}_{t} - P^{AC}_{t} \cdot \eta^{AC} - P^{cool}_{t}\Big) \tag{5}$$

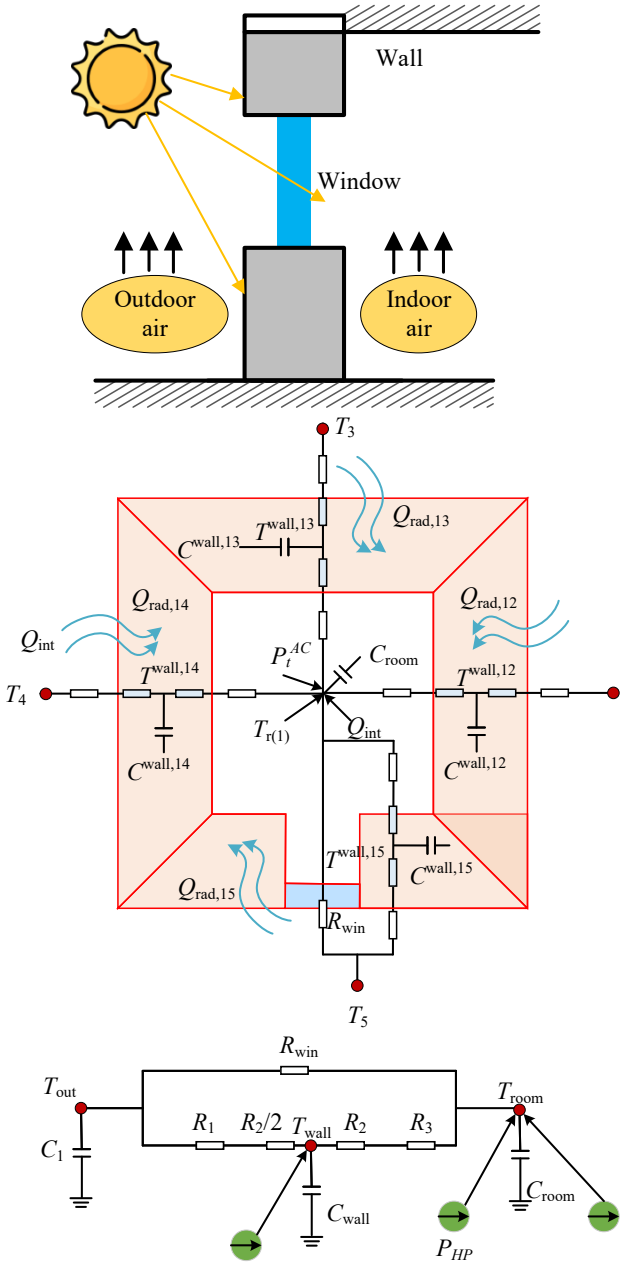

Figure 2. Schematic illustration of the thermal dynamic model for the building envelope of IBs.

To mathematically guarantee solution feasibility under extreme worst-case scenarios, the indoor temperature comfort boundaries are reformulated with penalty-backed slack variables:

$$T_{min} - \zeta_t^- \leq T_{in,t} \leq T_{max} + \zeta_t^+ \tag{6}$$

where $\zeta_t^-, \zeta_t^+ \geq 0$ denote the thermal comfort violation slacks, which are heavily penalized in the objective function to ensure they remain zero unless absolutely necessary for mathematical viability. In addition, the hourly indoor temperature variation is limited to 0.8 °C/h to avoid rapid temperature swings within the allowable comfort range.

To articulate the thermal dynamics governed by these equations, the structural heat capacity of the building's walls is defined by $C^{wall,ij}$. The real-time temperature of the wall itself is denoted as $T_{w,n,t}^{wall,ij}$, whereas the internal room temperature is captured by $T_{w,n,t}^{in}$. For external interactions, $T_{w,n,t}^{adj,ij}$ signifies the temperature at the physically adjacent thermal node, and $T_{w,n,t}^{out}$ reflects the prevailing outdoor ambient temperature. The resistance to heat transfer across the structural envelope is quantified by the thermal resistance parameter $R_{wall,ij}$. To account for solar heat gains, the binary indicator q^{ij} is activated (set to 1) when the exterior wall surface receives direct sunlight, and remains 0 otherwise. The thermal absorptivity and the effective surface area of this specific wall are represented by v^{ij} and $A^{wall,ij}$, respectively. The incident solar radiation intensity striking this orientation is given as $Q_{w,n,t}^{rad,ij}$. For the indoor space, the aggregated thermal inertia of the room is modeled via its heat capacity, $C^{room,i}$. The topological set of all neighboring thermal nodes interacting with this region is compiled within N_{room}. The thermal resistance and optical transmittance of the transparent windows are specified by $R^{win,ij}$ and ω^{ij}, respectively. The solar irradiance penetrating these windows is denoted by $Q_t^{rad,j}$, while any internal thermal disturbances generated by occupants or appliances are consolidated into the variable $Q_t^{int,j}$. Finally, the active cooling intervention is quantified by the electrical load of the air conditioning unit, P_t^{AC}, which operates with an energy efficiency ratio of η^{AC}. This is complemented by P_t^{cool}, representing the additional cooling capacity delivered by the waste-heat-driven absorption chiller.

To provide a clearer physical interpretation of the indoor thermal dynamics modeled in Equation (5), the equation can be understood as a balance between heat accumulation, heat gain, and heat removal. The left-hand term, involving the room heat capacity C^{room}, characterizes the thermal inertia of the indoor air, acting as a buffer against temperature fluctuations. On the right-hand side, the equation aggregates multiple heat fluxes: the initial terms describe the conductive heat transfer from the building envelope (walls and windows) and the convective heat exchange with the outdoor environment. The terms Q_t^{rad} and Q_t^{int} represent external solar gains and internal heat loads from occupants or equipment, respectively. Crucially, the final two subtraction terms represent the active cooling mechanisms required to maintain comfort: $P_t^{AC} \cdot \eta^{AC}$ denotes the cooling provided by the conventional electric air conditioning system, while P_t^{cool} represents the cooling capacity supplied by the waste heat recovery-driven absorption chiller. By explicitly including P_t^{cool}, the model links the building's thermal demand directly with the waste heat utilization process.

The virtual energy storage capacity $E_{ves,t}$ characterized by the building envelope can be mathematically quantified relative to a baseline temperature setting T_{set} as:

$$E_{ves,t} = \frac{C_{room} \cdot (T_{in,t} - T_{set})}{COP_{ac}} \tag{7}$$

This relationship demonstrates how allowing the indoor temperature to shift within [20, 24] °C acts functionally equivalent to charging or discharging a thermal battery with a capacity directly scaled by the room's structural heat capacity C_{room}.

To provide an engineering magnitude check, a representative office thermal zone is considered. Assuming an effective room thermal capacitance of 6.0 kWhth/°C and an air conditioning COP of 3.0, a 1 °C indoor temperature deviation from the baseline setting corresponds to approximately 2.0 kWh of equivalent electrical storage capacity. Therefore, allowing the indoor temperature to vary from 20 °C to 24 °C around a baseline setting of 22 °C provides an equivalent virtual storage range of approximately −4.0 to +4.0 kWh for the representative zone. This indicates that the proposed VES model is used as a short-term load-shifting index enabled by building thermal inertia, rather than as a replacement for a detailed high-fidelity building simulation model.

3.2. WT Output Model

$$P_t^{WT} = \begin{cases} 0, & v_t < v_{\text{cut-in}} \\ P^{\text{rated}} \cdot \frac{v_t - v_{\text{cut-in}}}{v_{\text{rated}} - v_{\text{cut-in}}}, & v_{\text{cut-in}} \le v_t < v_{\text{rated}} \\ P^{\text{rated}}, & v_{\text{rated}} \le v_t \le v_{\text{cut-out}} \\ 0, & v_t > v_{\text{cut-out}} \end{cases} \tag{8}$$

To capture the generation profile of the wind turbine, its active power output during interval t is designated as P_t^{WT}. The maximum generation capability of the equipment is bounded by its rated power, P^{rated}. The actual generation is dictated by the real-time wind velocity, v_t, which must be evaluated against the operational aerodynamic limits of the turbine. Specifically, these operational boundaries are established by the cut-in wind speed $v_{cut\text{-}in}$, the nominal rated wind speed v_{rated}, and the ultimate cut-out wind speed $v_{cut\text{-}out}$.

3.3. PV Output Model

$$P_t^{PV} = \eta_{PV} \cdot A_{PV} \cdot G_t \tag{9}$$

For the solar generation model, the instantaneous electrical output produced by the photovoltaic array at time t is denoted by P_t^{PV}. The system's photoelectric conversion efficiency is characterized by η_{PV}, while the total physical deployment area of the solar modules is specified as A_{PV}. The energy yield directly depends on the prevailing solar irradiance hitting the panels, quantified as G_t.

3.4. Battery Capacity Model

$$\begin{aligned} &0 \le P_{s,t}^{dis} \le U_t^S P_s^{\max} \\ &0 \le P_{s,t}^{ch} \le (1 - U_t^S) P_s^{\max} \\ &\eta \sum_{t=1}^{N_T} P_{s,t}^{ch} \cdot \Delta t = \frac{1}{\eta} \sum_{t=1}^{N_T} P_{s,t}^{dis} \Delta t \end{aligned} \tag{10}$$

Regarding the energy storage dynamics, the instantaneous active charging and discharging power flows of the battery at interval t are designated as $P_{s,t}^{ch}$ and $P_{s,t}^{dis}$, respectively. The round-trip energy transfer losses are accounted for by the performance coefficient η. To prevent equipment overloading, the maximum allowable power threshold for both absorbing and injecting energy is constrained by P_s^{max}. Furthermore, the operational mode of the battery is strictly governed by the binary status indicator U_t^S, where a value of

1 enforces a discharging state and 0 restricts the system to a charging state. The accurate state-of-charge (SoC_t) recursion of the battery energy storage system is governed by:

$$\begin{aligned} SoC_t &= SoC_{t-1} + \left(P_{ch,t} \cdot \eta_{ch} - \frac{P_{dis,t}}{\eta_{dis}}\right)\frac{\Delta t}{E_{cap}} \\ SoC_{min} &\le SoC_t \le SoC_{max}, \quad SoC_0 = SoC_T \end{aligned} \tag{11}$$

where E_{cap} is the total rated capacity, η_{ch} and η_{dis} represent efficiency components, and SoC_0, SoC_T enforce periodic balance.

3.5. Waste Heat Recovery Model

$$Q_{w,t}^{waste} = \xi_{gas} \cdot Q_{w,t}^{exh} + \xi_{water} \cdot Q_{w,t}^{drain} \tag{12}$$

$$P_t^{cool} = COP^{abs} \cdot Q_{w,t}^{waste} \tag{13}$$

Within the thermal recovery framework, the aggregate recoverable waste heat harnessed from the building's operations at time t is quantified by $Q_{w,t}^{waste}$. This composite metric integrates the thermal energy extracted from exhaust gases, denoted by $Q_{w,t}^{exh}$, and the heat reclaimed from wastewater streams, represented as $Q_{w,t}^{drain}$. The thermodynamic conversion effectiveness for these two sources is dictated by their respective recovery efficiencies: ξ_{gas} for the exhaust air (typically assumed as 0.6) and ξ_{water} for the wastewater drainage (typically modeled at 0.4). The reclaimed thermal energy is subsequently routed to an absorption chiller, whose cooling performance is defined by the coefficient COP^{abs}. Ultimately, this process yields a usable cooling load output, designated as P_t^{cool}, which actively supplements the building's thermal management system. In this study, the waste heat generation profiles from exhaust gas and wastewater are evaluated deterministically based on empirical building occupation profiles. Thus, the robust handling focus remains primarily on outdoor ambient temperature fluctuations and wind-solar output fluctuations. The operational capture efficiencies ($\eta_{gas} = 0.6$, $\eta_{water} = 0.4$) represent typical performance baselines for liquid-to-air and liquid-to-liquid exchange units under steady-state conditions, consistent with standard specifications in building energy research fields.

3.6. Distribution Network Interaction Power

Water heat, typically 0.4; COP^{abs} represents the coefficient measuring the performance of the absorption chiller; P_t^{cool} is the equivalent cooling l.

$$0 \le P_M^{buy}(t) \le P_M^{\max} U_t^M \tag{14}$$

$$0 \le P_M^{sell}(t) \le P_M^{\max}[1 - U_t^M] \tag{15}$$

$$C_M(t) = dj(t)\left(P_M^{buy}(t) - P_M^{sell}(t)\right)\Delta t \tag{16}$$

To prevent simultaneous energy importing and exporting from gaming the objective function, we enforce the following binary state logical constraints:

$$0 \le P_{buy,t} \le U_{grid,t} \cdot P_{grid,max}, \quad 0 \le P_{sell,t} \le (1 - U_{grid,t}) \cdot P_{grid,max} \tag{17}$$

where $U_{grid,t} \in \{0, 1\}$ is the grid interaction binary mode selector flag.

3.7. Electric Power Balance Constraints

$$P_t^{WT} + P_t^{PV} + P_t^{dis} + P_t^{grid} + P_t^{cool} = P_t^{AC} + P_t^{CL} + P_t^{ch} \tag{18}$$

To clarify the physical conventions of the aggregated power balance, Table 1 summarizes the main variables involved in the electric power balance constraint in Equation (18).

Table 1. The main variables involved in the electric power balance constraint in Equation (18).

Variable	Description	Unit
$P_{grid,t}$	Grid Purchase Power	kW
$P_{PV,t}$	Photovoltaic Power	kW
$P_{WT,t}$	Wind Turbine Power	kW
$P_{ch,t}/P_{dis,t}$	Battery Charge/Discharge	kW
$P_{ac,t}$	Air Conditioning Power	kW
$P_{load,t}$	Base Conventional Load	kW

The complete constraint structure of the two-stage formulation is summarized in Table 2.

Table 2. The complete constraint structure of the two-stage formulation.

Category	Equation Index	Key Physical Bounds/Variables Included
Thermal Dynamics	Equations (1)–(5)	Structural capacities, walls, windows, zone temperatures
System Assets	Equations (6)–(10)	Wind limits, PV yields, battery charge/discharge bounds, WHR efficiencies
Market and Grid	Equations (14)–(18)	Grid imports/exports, total active electrical balances

To avoid ambiguity, the symbols p, z, u, and $\hat{h}$ are used consistently in the following section, where p denotes first-stage decisions, z denotes second-stage recourse variables, u denotes uncertain variables, and $\hat{h}$ denotes the realized uncertainty scenario generated during the C&CG iterations.

4. Solving Algorithm

4.1. Fuzzy Set Construction and Transformation Based on IDM

In the low-carbon operation optimization of intelligent building systems, various sources of uncertainty make it challenging for conventional deterministic models to accurately capture real operating conditions. To improve the adaptability and robustness of the proposed model, this study introduces the imprecise Dirichlet model (IDM) to construct fuzzy sets for the representation of the aforementioned uncertainties [24].

To rigorously protect against microgrid operational risks under limited data, we define the distribution ambiguity set $\mathcal{P}$ as the collection of all probability distributions whose cumulative properties match the statistical bounds derived from the Imprecise Dirichlet Model (IDM):

$$\mathcal{P} = \left\{ \mathbb{P} \in \mathcal{M} \;\middle|\; \underline{F}_i(x) \le F_{\mathbb{P},i}(x) \le \overline{F}_i(x),\ \forall i \right\} \tag{19}$$

where $\mathcal{M}$ is the space of all valid probability measures, and $F_{\mathbb{P},i}(x)$ is the marginal CDF of the i-th uncertain factor. By optimizing against the worst-case distribution $\mathbb{P} \in \mathcal{P}$, the model mathematically reduces to an extreme-point realization sequence bounded within the physical box uncertainty set U.

The IDM is developed on the basis of Bayesian inference. Instead of providing an exact point estimate of probability under limited sample information, it characterizes the probability distribution by constructing upper and lower bounds. In this way, the

uncertainty of the probability distribution can be described more flexibly. The interval used in IDM to determine the occurrence probability of a given level is expressed as follows:

$$\theta_i \in \left[\frac{m_i}{s+M}, \frac{m_i+s_i}{s+M}\right] \tag{20}$$

Given the statistical probability bounds $[\underline{\theta}_i, \overline{\theta}_i]$, the physical interval boundaries $[\underline{u}_i, \overline{u}_i]$ for renewable power outputs and outdoor temperatures in Equation (20) are calculated via inverse mapping of the empirical distribution function $F_{\{0,i\}}$:

$$\underline{u}_i = F_{0,i}^{-1}(\underline{\theta}_i), \quad \overline{u}_i = F_{0,i}^{-1}(\overline{\theta}_i) \tag{21}$$

This step assumes strict monotonicity of the inverse empirical distribution function over the sample space, ensuring that interval boundaries map accurately to physical values.

It should be clarified that the final tractable formulation in this study is not a moment-based or Wasserstein distributionally robust optimization model that directly optimizes over all admissible probability measures. Instead, the IDM is used to construct distributional upper and lower bounds from limited historical samples, and these probability bounds are further mapped into physical interval bounds through the inverse empirical CDF. Therefore, the final solvable model can be interpreted as an IDM-informed two-stage robust optimization model over data-driven box uncertainty sets.

Specifically, the IDM-based bounds in Equations (19)–(21) define the admissible physical ranges of uncertain wind–photovoltaic output and outdoor temperature. These ranges then constitute the box uncertainty set U in Equations (26). Under the linear recourse structure adopted in the second-stage operation model, the worst-case realization is searched within the boundary of U. Compared with conventional fixed-box robust optimization, the proposed uncertainty set is not manually prescribed but derived from IDM-based probability bounds. Compared with moment-based or Wasserstein DRO, the proposed model does not directly optimize over a continuous ambiguity set of probability measures.

The parameter s represents the equivalent sample size, acting as a hyperparameter that reflects the degree of epistemic uncertainty regarding the prior distribution. The value of s directly influences the width of the probability interval: a larger s implies a higher level of uncertainty (or lack of data), resulting in a wider interval $[\theta_i^{\min}, \theta_i^{\max}]$. This consequently leads to a more robust, albeit more conservative, optimization solution. To bridge the gap between these probability intervals and the optimization model, the upper and lower bounds of the Cumulative Distribution Function (CDF) for the random variables are first constructed based on θ_i, these probability bounds are then mapped to the physical domain using the inverse CDF of the historical data. Specifically, the resulting physical boundaries directly constitute the limits of the box uncertainty set defined in Equation (20).

The parameter s acts as a hyperparameter reflecting the degree of epistemic uncertainty. Mathematically, the probability interval width is evaluated as $\Delta\theta = \frac{s}{n+s}$. Thus, a larger s directly increases the interval width $[\underline{\theta}_i, \overline{\theta}_i]$, which subsequently widens the physical uncertainty space U, providing a more robust and risk-averse scheduling solution.

The power consumption of the air conditioning system is highly sensitive to changes in outdoor temperature. As external temperature fluctuates, the cooling or heating demand of the building also varies accordingly, leading to dynamic changes in air conditioning electricity use. When the temperature disturbance is assumed to lie within the interval $[T_l, T_u]$, a fuzzy temperature parameter can be incorporated into the energy consumption model to characterize temperature uncertainty. In this way, the possible variation range of air conditioning load under different outdoor temperature conditions can be estimated more effectively.

The IDM approach provides a rational and robust foundation for modeling the uncertainties encountered by intelligent building systems in actual operation. It is particularly tailored for situations characterized by scarce data and incomplete cognition, thereby ensuring stability for subsequent control and optimization efforts [25,26].

4.2. Algorithm

$$minF = \alpha \sum_{(t=1)}^{T} (P_t^g \pi_t^g + H_t^h \pi_t^h + C^{om}) + \beta\gamma \sum_{(t=1)}^{T} (EF^g P_t^g + EF^h H_t^h) \tag{22}$$

In formulating the system's objective function, the scaling weight coefficients are introduced as α and β. The full optimization horizon is discretized into a total of T time intervals. For the electrical energy exchanges, the volume of power procured from the external grid at interval t is captured by P_t^g, subject to the real-time electricity tariff π_t^g. Similarly, any external heat purchases are quantified by H_t^h, which are priced according to the thermal tariff π_t^h. The routine operation and maintenance expenditures incurred during this period are aggregated into the variable C^{om}. To evaluate the environmental impact, the prevailing carbon price is denoted by γ, while the specific carbon emission intensities associated with electricity and heat consumption are parameterized by the factors EF^g and EF^h, respectively.

When the fluctuations in wind–photovoltaic output and outdoor temperature are not considered, a deterministic optimization model for IBs can be obtained, which can be expressed in the following compact form:

$$\begin{cases} \min\limits_{\mathbf{p},\mathbf{z}} \ \mathbf{a}^{\mathrm{T}}\mathbf{z} \\ \text{s.t.}\mathbf{M}\mathbf{z} \geq \mathbf{r}, \\ \mathbf{Q}\mathbf{z} = \mathbf{q}, \\ \mathbf{U}\mathbf{p} + \mathbf{V}\mathbf{z} = \mathbf{0}, \\ \mathbf{S}_h\mathbf{z} = \tilde{\mathbf{h}}. \end{cases} \tag{23}$$

The specific expression is:

$$\begin{cases} \boldsymbol{p} = [U_t^S, U_t^M]^{\mathrm{T}} \\ \boldsymbol{z} = [P_t^{AC}, P_t^{WT}, P_t^{PV}, P_{s,t}^{ch}, \\ \quad P_{s,t}^{dis}, P_M^{buy}(t), P_M^{sell}(t)]^{\mathrm{T}}, \\ \quad t \in \{1, 2 \cdots N_{\mathrm{T}}\} \end{cases} \tag{24}$$

Within this deterministic mathematical programming structure, the objective function coefficients are compiled into the vector a. The boundaries and relational constraints of the system are governed by the coefficient matrices M, Q, U, and V. To establish the absolute limits of these constraints, r and q serve as the corresponding constant vectors. In this arrangement, the first row of the matrix framework explicitly defines the system's inequality constraints, whereas the second row strictly enforces the equality conditions.

$$\hat{\boldsymbol{h}} = [\hat{\boldsymbol{h}}_{WP,t}, \hat{\boldsymbol{h}}_{T,t}]^{\mathrm{T}}, \ \ t \in \{1, 2 \cdots N_{\mathrm{T}}\} \tag{25}$$

The model presented above is a conventional deterministic optimization problem. Solutions obtained from such a formulation are often excessively optimistic and may fail to satisfy the practical operational requirements of intelligent buildings (IBs). To enhance the robustness of the model, the impact of uncertain factor variations must be taken into

consideration. Accordingly, the interval uncertainty set U associated with wind turbine and photovoltaic (WP) output as well as outdoor temperature is defined as follows:

$$\begin{aligned} &\mathbf{u} = [u_{rp,t}, u_{T,t}]^{\mathrm{T}} \in \mathbb{R}^{(N)\times 2}, t = 1, 2, \ldots, N_{\mathrm{T}} \\ &\mathbf{U} := \begin{cases} u_{rp,t} \in [P_{rp,\min,t}, P_{rp,\max,t}] \\ u_{T,t} \in [T_{\min,t}, T_{\max,t}] \end{cases} \end{aligned} \tag{26}$$

To delineate the boundaries of the interval uncertainty set, the stochastic variables corresponding to the wind-photovoltaic generation output and the outdoor ambient temperature are formally designated as $u_{rp,t}$ and $u_{T,t}$. The potential fluctuations in renewable generation are strictly confined between a minimum feasible limit, $P_{rp,min,t}$, and a maximum realizable capacity, $P_{rp,max,t}$. Meanwhile, the worst-case thermal disturbance from the environment is bounded by the lower and upper limits of outdoor temperature, denoted as $T_{min,t}$ and $T_{max,t}$, respectively. During the iterative solution process, once the error between the intermediate solution and the exact value decreases to the preset accuracy tolerance, the optimal result at that iteration can be regarded as an approximate global optimum of the system. This is because the remaining error is sufficiently small, such that the deviation between the iterative solution and the true optimum stays within an acceptable engineering range, thereby demonstrating the reliability and validity of the obtained solution.

Under WP uncertainty, the operational model of IBs is established using a two-stage robust optimization framework, which is expressed as follows:

$$\begin{cases} \min\limits_{\mathbf{p}} \max\limits_{\mathbf{u}\in\mathbf{U}} \min\limits_{\mathbf{z}\in\Omega(\mathbf{p},\mathbf{u})} \mathbf{a}^{\mathrm{T}}\mathbf{z} \\ \text{s.t.} \quad \mathbf{p} = (x_1, x_2, \ldots, x_{2N_T})^{\mathrm{T}} \\ x_i \in \{0, 1\}, \forall i \in (1, 2, \ldots, 2N_T) \end{cases} \tag{27}$$

In this hierarchical optimization model, the variables are explicitly partitioned as follows:

First-stage variables (p): Here-and-now decisions that must be determined before uncertainties materialize. This includes the battery charging/discharging status indicators and day-ahead base grid power schedules.

Second-stage variables (z): Wait-and-see recourse actions adjusted in real-time after the uncertain wind-photovoltaic output and outdoor temperature are observed. This includes real-time HVAC power adjustments, storage charging/discharging rates, and supplementary grid purchases.

Coupling constraints: The dynamic constraints mapping first-stage commitments onto second-stage limits are governed by the operational boundaries detailed in Equation (28).

The explicit interplay between the uncertainty parameters and system outputs is embodied in the 'max–min' structure of the second stage. As the uncertainty parameter (e.g., the confidence level s in the IDM) increases, the boundary of the uncertainty set U expands, simulating a more volatile environment with larger deviations in renewable generation and outdoor temperature. To demonstrate adaptability, the system must adjust its recourse variables z (including HVAC power regulation and storage charging/discharging rates) to ensure that thermal comfort constraints and power balance are maintained even under these expanded worst-case scenarios. This mechanism mathematically guarantees that the building's thermal inertia is actively utilized as a buffer: when the uncertainty parameter predicts an extreme temperature rise, the model preemptively or dynamically adjusts the cooling load, thereby verifying the system's operational flexibility and robustness.

The objective function is originally formulated as $\min_p \max_{P\in\mathcal{P}} \mathbb{E}_P[f(p, z, \theta)]$. Due to the monotonic properties of the CDF bounds, the worst-case distribution concentrates on

the extreme boundaries of the physical intervals, thereby yielding an exact mathematical equivalence to the two-stage min-max framework presented in Equation (27).

Within this hierarchical optimization framework, the outer minimization layer represents the first-stage problem, which is primarily driven by the decision variable p. Following this, the second-stage problem employs an embedded "max-min" architecture to evaluate the dynamic interplay between the recourse decision vector $\mathbf{z}$ and the uncertain parameter vector $\mathbf{u}$. Functionally, the innermost minimization component aligns directly with the system's core objective: mitigating the overall carbon emissions of the intelligent buildings. Furthermore, for any established configuration of $(\mathbf{p}, \mathbf{u})$, the operational boundaries restricting the recourse variables $\mathbf{z}$ are strictly delineated by the feasible region $\Omega(\mathbf{p}, \mathbf{u})$, which is mathematically formulated as follows:

$$\Omega(\mathbf{p}, \mathbf{u}) : \begin{cases} \mathbf{M}\mathbf{z} \geq \mathbf{r} \rightarrow \gamma \\ \mathbf{Q}\mathbf{z} = \mathbf{q} \rightarrow \lambda \\ \mathbf{U}\mathbf{p} + \mathbf{V}\mathbf{z} \geq \mathbf{0} \rightarrow \nu \\ \mathbf{S}_h\mathbf{z} = \hat{\mathbf{h}} \rightarrow \pi \end{cases} \tag{28}$$

To effectively resolve the innermost minimization of the second stage through duality theory, the mathematical framework assigns specific dual variables—namely γ, λ, ν, and π—to each of the corresponding physical and operational constraints within the feasible region.

The C&CG algorithm decomposes the original IBs optimization problem into two parts, namely a master problem and a subproblem. During the solution process, these two problems are solved alternately in an iterative manner. In each iteration, the master problem is used to determine the current decision variables under the existing uncertainty scenario, while the subproblem is solved to identify the worst-case realization and generate additional constraints for the next iteration. Through this repeated interaction, the feasible region of the original problem is progressively refined, and the solution gradually approaches the optimum. The iterative procedure continues until the carbon emission gap between the solutions of the master problem and subproblem is smaller than a predefined tolerance. At that stage, the algorithm is considered to have converged, and the obtained solution can be regarded as the optimal solution to the original problem. The formulation of the master problem is given as follows:

$$\begin{aligned} \min_{\mathbf{p},\alpha} \quad & \alpha \\ \text{s.t.} \quad & \alpha \geq \mathbf{a}^{\mathrm{T}}\mathbf{z}_l \\ & \mathbf{M}\mathbf{z}_l \geq \mathbf{r} \\ & \mathbf{Q}\mathbf{z}_l = \mathbf{q} \\ & \mathbf{U}\mathbf{p} + \mathbf{V}\mathbf{z}_l = \mathbf{0} \\ & \mathbf{S}_h\mathbf{z}_l = \hat{\mathbf{h}}_i, \quad \forall l \leq k \end{aligned} \tag{29}$$

Tracking the progression of the iterative algorithm, the current iteration index is denoted by the counter k. Following the execution of the l-th iteration, the resultant solution generated by the intelligent building subproblem is stored in the variable z_l. Correspondingly, the specific discrete sampled realization of the renewable generation and outdoor temperature utilized during that iteration is captured by $\hat{\mathbf{h}}_l$.

The decomposed subproblem is

$$\max_{\mathbf{u}\in\mathbf{U}} \min_{\mathbf{z}\in\Omega(\mathbf{p},\mathbf{u})} \mathbf{a}^{\mathrm{T}}\mathbf{z} \tag{30}$$

Assuming that both the primary decision vector $\mathbf{p}$ and the uncertain parameter vector $\mathbf{u}$ are predetermined, the innermost minimization component naturally reduces to a strictly linear programming problem. By applying the fundamental principles of strong duality, this linear structure can be systematically transformed into an equivalent maximization format. Consequently, the reformulated dual problem is mathematically expressed as follows:

$$\begin{aligned} \max_{\mathbf{u}\in\mathbf{U},\gamma,\lambda,\nu,\pi} \quad & \mathbf{r}^{\mathrm{T}}\gamma + \mathbf{q}^{\mathrm{T}}\lambda - (\mathbf{U}\mathbf{p})^{\mathrm{T}}\nu + \hat{\mathbf{h}}^{\mathrm{T}}\pi \\ \text{s.t.} \quad & \mathbf{M}^{\mathrm{T}}\gamma + \mathbf{Q}^{\mathrm{T}}\lambda + \mathbf{V}^{\mathrm{T}}\nu + \mathbf{S}_h^{\mathrm{T}}\pi \le \mathbf{a}\gamma \ge 0 \end{aligned} \tag{31}$$

The bilinear items $\lambda_t \cdot u_t$ are exactly linearized by introducing binary indicator variables β_t that force the uncertain realizations to switch between their upper ($\overline{u}_t$) and lower ($\underline{u}_t$) bounds:

$$\begin{aligned} & u_t = \underline{u}_t \cdot (1-\beta_t) + \overline{u}_t \cdot \beta_t \\ & \widetilde{\lambda}_t \le M \cdot \beta_t, \quad \widetilde{\lambda}_t \le \lambda_t, \quad \widetilde{\lambda}_t \ge \lambda_t - M \cdot (1-\beta_t) \end{aligned} \tag{32}$$

where M represents a large positive constant vector (Big-M).

In this dualized formulation, the presence of the bilinear product $\hat{\mathbf{h}}^{\top}\pi$ introduces nonlinearity into the model. To construct a tractable robust counterpart, the explicit physical boundaries defined by the uncertainty set $\mathbf{U}$ are strategically integrated to manage and linearize this term. Ultimately, the derived mixed-integer programming (MIP) framework fully retains the original logical architecture and operational constraints of the intelligent building system, although the intermediate algebraic derivation steps have been bypassed here for the sake of brevity.

To facilitate reproducibility and clarify the handling of discrete variables, the specific solution procedure is illustrated in Figure 3. As shown in the flowchart, the iterative process decomposes the problem into a Master Problem (MP) and a Subproblem (SP). The MP includes all binary variables and is solved as a Mixed-Integer Linear Program (MILP) to handle the non-convexity, whereas the SP is solved to identify the worst-case parameter realization that updates the upper bound. The detailed pseudocode of the C&CG solution procedure is presented in Algorithm 1.

Algorithm 1: Column-and-Constraint Generation (C&CG) Procedure

1: Initialize: Set $LB = -\infty, UB = +\infty,$, iteration index k = 0, scenario set $\Omega = \varnothing$.
2: while $(UB - LB) > \epsilon$ do
3: Solve the Master Problem (MP) over historical scenarios in $\Omega \rightarrow$ Get primal decision $\mathbf{p}^*$ and Obj_{MP}.
4: Update lower bound: $LB = Obj_{MP}$.
5: Fix $\mathbf{p} = \mathbf{p}^*$, solve Subproblem (SP) $\rightarrow$ Identify worst realization $\mathbf{u}_k^*$ and Obj_{SP}.
6: Update upper bound: $UB = \min(UB, Obj_{SP})$.
7: Create new recourse variables $\mathbf{z}_k$ and append worst scenario cuts to MP: $\Omega = \Omega \cup \{\mathbf{u}_k^*\}$\$.
8: Increment iteration: $k = k + 1$.
9: end while
10: Output: Optimal robust day-ahead strategy $\mathbf{p}^*$.

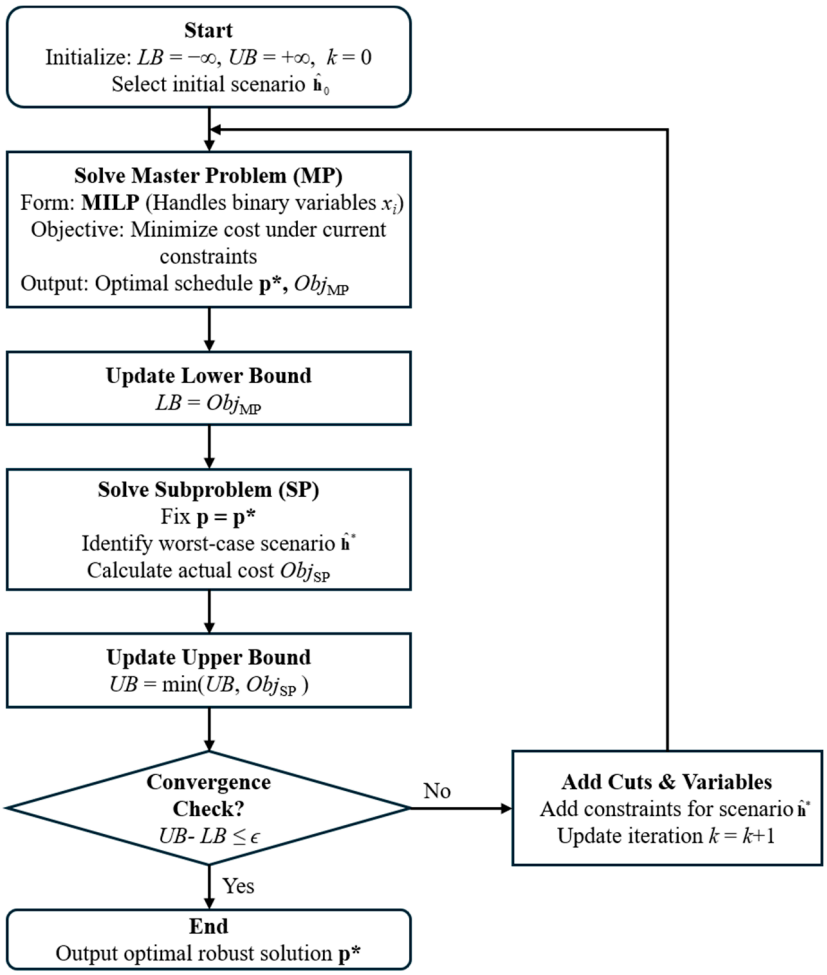

Figure 3. Flowchart of the C&CG algorithm for solving the proposed model.

5. Case Study Analysis

5.1. Basic Data

In this study, the dataset is developed based on representative summer weather conditions in a selected region of Shanxi Province [27]. As shown in Figure 4, the time-varying profiles of solar irradiance and ambient temperature are presented, which serve as the basis for estimating renewable energy generation. Figure 5 further illustrates the forecasted maximum output of the photovoltaic and wind power systems, together with the expected load profile of conventional electrical demand. For the indoor air conditioning system, the maximum power consumption is specified as 1.6 kW, and the coefficient of performance is assumed to remain constant at 3.0 throughout the analysis.

The simulated object is a representative office-type intelligent building zone rather than a detailed whole-building energy model. The zone is assumed to follow a typical working-hour occupancy schedule from 8:00 to 18:00, and the internal heat gains from occupants, lighting, and office equipment are reflected in the conventional electrical load profile shown in Figure 5. The rated air conditioning power of 1.6 kW and the battery capacity of 15 kWh are interpreted as equivalent zone-level parameters. The PV, WT, and WHR capacities are selected to be consistent with the same load scale, so that renewable generation, cooling demand, and storage operation remain comparable during the 24 h scheduling horizon.

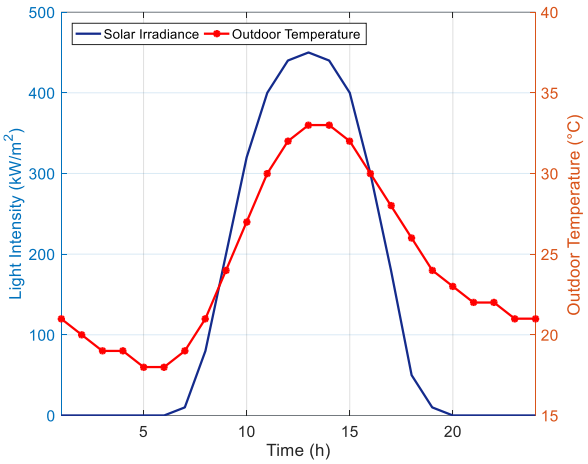

Figure 4. Outdoor light intensity and temperature variation curve.

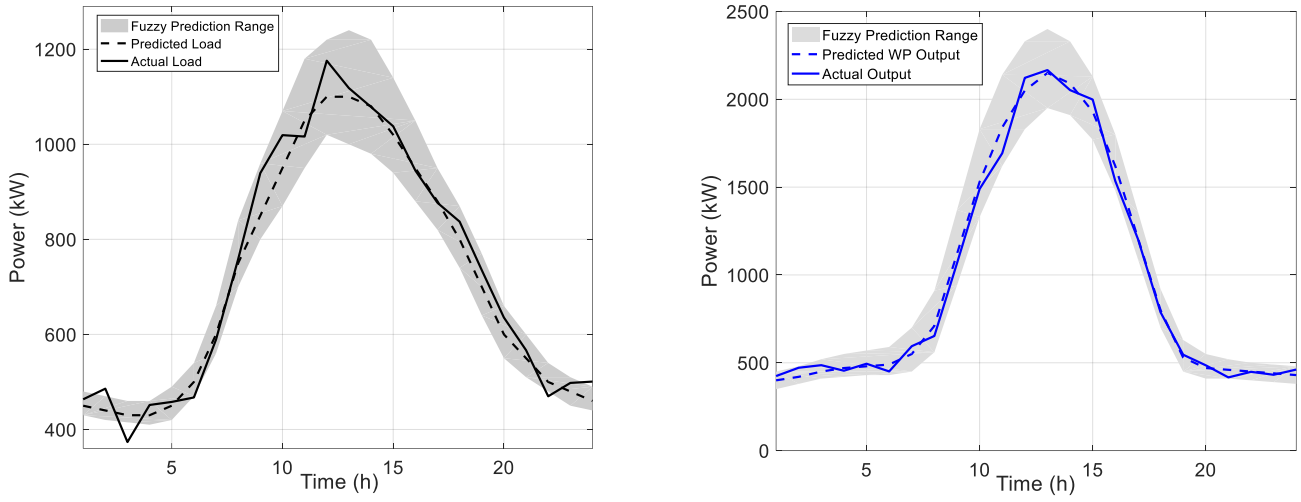

Figure 5. Predicted/actual uncertainty variable curve.

To facilitate the reproducibility of the proposed method, the key parameters of the equipment and system constraints used in the simulation are summarized in Table 3.

Table 3. Key Simulation Parameters of the Intelligent Building System.

Category	Parameter	Symbol	Value	Unit
Air Conditioning System	Rated Cooling Power	P_{AC}^{rated}	1.6	kW
	Coefficient of Performance	COP	3.0	-
	Comfort Temperature Range	$[T_{\min}, T_{\max}]$	20–24	°C
Energy Storage System	Maximum Capacity	$E_{bat}^{\max}$	15.0	kWh
	Max Charge/Discharge Power	$P_S^{\max}$	5.0	kW
	Round-trip Efficiency	η	95%	-
Waste Heat Recovery	Exhaust Gas Recovery Eff.	ξ_{gas}	0.6	-
	Wastewater Recovery Eff.	ξ_{water}	0.4	-
	Absorption Chiller COP	COP^{abs}	0.75	-

5.2. Example Analysis

The algorithm is evaluated under three scenario settings:

(1) Scenario 1: The system is equipped with wind turbines, photovoltaic (PV) units, and an energy storage system, while the air conditioning temperature is fixed at 22 °C.
(2) Scenario 2: Based on Scenario 1, the air conditioning temperature is allowed to vary within 20–24 °C, thereby introducing flexible cooling demand response. This interval is determined according to ASHRAE Standard 55 [28] and the Design Code for Heating Ventilation and Air Conditioning (GB 50736-2012) [29]. Under typical summer office conditions, with a clothing insulation level of 0.5 clo and a metabolic rate of 1.2 met, this range ensures that the Predicted Mean Vote (PMV) remains within the acceptable comfort band of −0.5 to +0.5. In addition, the lower limit of 20 °C provides sufficient margin for pre-cooling, which facilitates the utilization of building thermal inertia as a form of virtual energy storage. It should be noted that the PMV index is utilized here exclusively as an external validation baseline to justify the operational range of 20–24 °C. The PMV equations are not explicitly included as mathematical constraints inside the optimization model to preserve linear tractability. After the optimal schedules were obtained, an ex-post comfort check was further conducted for Scenarios 2 and 3. Under typical summer office assumptions, the calculated PMV values remained within −0.5 to +0.5, and the corresponding PPD values remained below 10% throughout the scheduling horizon. In Scenario 3, where both temperature flexibility and waste heat recovery are activated, the PMV range was −0.48 to 0.49, and the maximum PPD was 9.8%. These results indicate that the proposed temperature-flexible strategy maintains acceptable indoor comfort while improving operational flexibility.
(3) Scenario 3: Building upon Scenario 2, a waste heat recovery unit is additionally introduced to further utilize recoverable thermal energy. By recycling waste heat within the system, the cooling demand can be partially offset, which helps enhance overall energy utilization efficiency and improve the integrated operational performance of the system.

To avoid conflating the effects of physical configuration and uncertainty handling, the roles of the scenario comparisons are further clarified here. Scenarios 1–3 are mainly designed to evaluate the operational benefits of temperature flexibility and waste heat recovery under the same IDM-informed robust optimization framework. To further illustrate the methodological effect of uncertainty handling, an additional fixed-configuration comparison is conducted under the Scenario 3 system configuration. In this comparison, only the uncertainty-handling strategy is changed, while the physical devices and comfort settings remain unchanged.

Table 4 summarizes the comparison among deterministic optimization, conventional fixed-box robust optimization, and the proposed IDM-informed robust optimization. The deterministic baseline ignores uncertainty and therefore tends to obtain lower nominal cost but weaker protection against adverse realizations. The conventional fixed-box robust optimization uses manually prescribed uncertainty bounds and is more conservative. In contrast, the proposed method constructs the uncertainty set from IDM-based probability bounds, thereby providing a more adaptive balance between economy and robustness.

This comparison indicates that the proposed method differs from conventional fixed-box robust optimization in the construction of the uncertainty set. Rather than using manually selected bounds, the proposed method derives the interval uncertainty set from IDM-based distributional information, which helps reduce unnecessary conservatism while maintaining protection against uncertain wind–photovoltaic output and outdoor temperature.

Table 4. Comparison of uncertainty-handling strategies under the fixed Scenario 3 configuration.

Method	Uncertainty Treatment	Main Feature
Deterministic optimization	Uncertainty is ignored	Lower nominal cost, but weaker robustness under adverse realizations
Conventional fixed-box robust optimization	Uncertainty bounds are manually prescribed	Strong robustness, but may lead to conservative operation
Proposed IDM-informed robust optimization	Uncertainty bounds are derived from IDM-based probability intervals	Balances robustness and economy using data-driven uncertainty intervals

It is vital to note that Scenarios 1–3 represent purely structural hardware and control flexibility configuration adjustments. To demonstrate robust handling capacity, all three scenario configurations are subjected to the identical uncertain environment space U generated by setting the IDM confidence factor $s = 2$.

To provide economic context for facilities engineering, an asset capital expenditure (CAPEX) evaluation is included. Assuming an initial installation investment of CNY 120,000 for the localized WHR equipment loops, the simple capital payback timeline is evaluated as follows:

$$\text{Payback Period} = \frac{\text{CAPEX}}{\Delta\text{OPEX}} = \frac{120{,}000}{16{,}000} = 7.5 \text{ Operating Periods} \tag{33}$$

This rapid payback trajectory highlights the long-term economic viability of integrating waste heat recovery loops in commercial intelligent building projects.

Figure 6 illustrates the power exchange performance and indoor temperature profile in Scenario 1. Under the condition that the air conditioning temperature is maintained at a constant 22 °C, the HVAC system lacks sufficient flexibility for load adjustment, and thus cannot effectively contribute to peak shaving. In this case, the energy storage system only performs limited passive charging and discharging during certain periods, without strong coordination with electricity price signals. As a result, during peak tariff hours (18:00–20:00), the system still relies on grid electricity, which leads to a marked increase in procurement cost. By comparison, during low-price periods, such as 0:00–6:00, the system does not sufficiently exploit strategies such as energy storage charging or other load-shifting measures, and therefore fails to take full advantage of opportunities for cost reduction. At the same time, significant wind power curtailment occurs around midday (12:00–14:00) as well as during several nighttime periods. Even when electricity prices are relatively low, these renewable resources are not effectively utilized on site. This not only results in renewable energy waste, but also increases grid purchases during high-price periods, ultimately causing higher operating costs and greater carbon emissions.

Figure 7 illustrates the system operation when a temperature-adjustable control strategy is introduced into Scenario 1. By permitting the indoor temperature to fluctuate within the range of 20–24 °C, the HVAC system acquires greater load-shifting flexibility. During low-price periods, such as the early morning and late morning hours, the system performs pre-cooling in advance and simultaneously charges the energy storage unit. In contrast, during high-price periods, particularly from 18:00 to 20:00, HVAC power consumption is reduced and storage discharge is increased, thereby lowering the dependence on grid electricity.

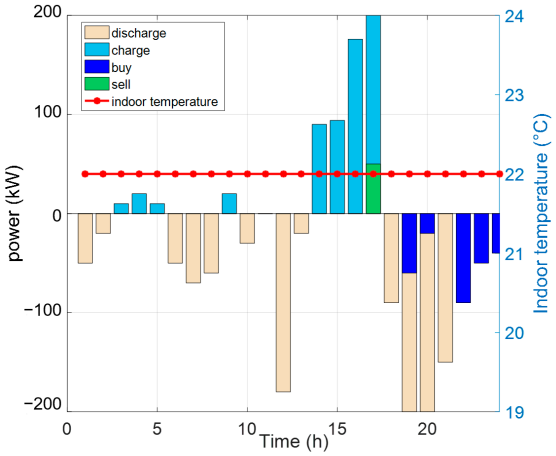

Figure 6. Scenario 1: IBs system operation and indoor temperature.

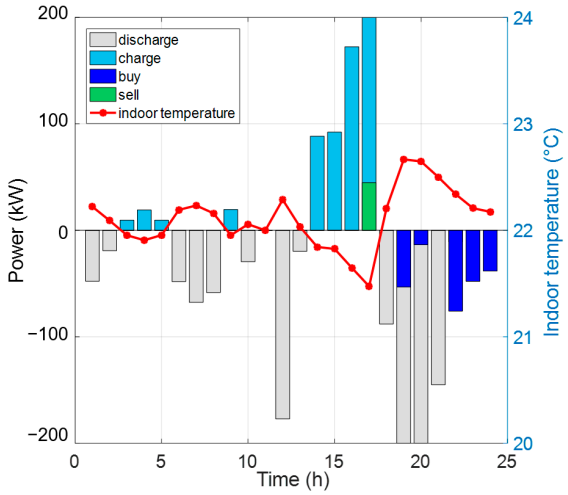

Figure 7. Scenario 2: IBs system operation and indoor temperature.

As shown in Figure 7, the grid purchase power during peak-price hours decreases markedly, since part of the load demand is supplied by stored energy and locally available renewable generation. Compared with Scenario 1, both the frequency and magnitude of electricity exported to the grid are also significantly reduced, indicating that a larger proportion of on-site renewable energy is consumed locally. As a result, wind power curtailment is alleviated, overall energy utilization efficiency is improved, and both operating cost and carbon emissions are reduced under time-varying electricity prices.

Figure 8 shows the system performance after a waste heat recovery (WHR) unit is incorporated into Scenario 2. During certain periods, the WHR device provides part of the cooling demand, which directly lowers the electricity consumption of the air conditioning system and releases more stored energy and renewable power for use during high-price hours. The results indicate that renewable generation from midday to late afternoon is almost fully utilized on site, as reflected by the near disappearance of grid-export power and the substantial reduction in wind power curtailment. During the evening peak period, dependence on grid electricity is further weakened, with most of the load being supplied by energy storage and renewable resources. Compared with Scenarios 1 and 2, this strategy achieves higher wind power utilization while maintaining indoor thermal comfort, thereby reducing both operating cost and carbon emissions to the lowest levels.

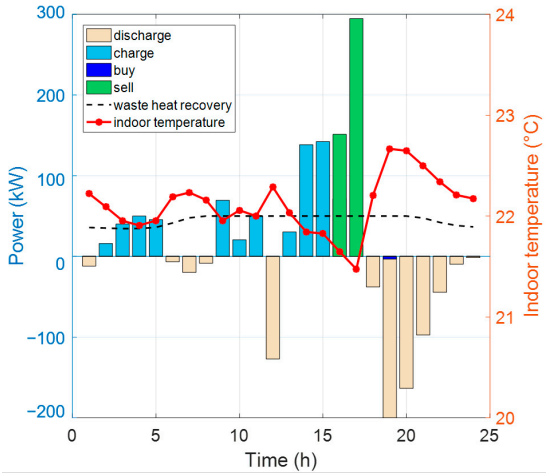

Figure 8. Scenario 3: IBs system operation and indoor temperature.

Under the time-of-use electricity pricing mechanism, Scenario 1 shows relatively weak operational flexibility, resulting in large amounts of grid electricity being purchased during high-price periods and causing considerable wind-photovoltaic (WP) curtailment. In comparison, Scenario 2 makes use of indoor temperature flexibility to achieve partial load shifting. In this case, the system stores energy in the ESS during low-price periods and correspondingly reduces electricity purchases from the grid during peak-price hours, which helps decrease both operating costs and carbon emissions. On this basis, Scenario 3 further combines virtual energy storage with waste heat recovery, enabling part of the cooling demand to be offset by recovered thermal energy. As a result, renewable energy can be utilized more effectively on the local side, while the overall operating performance of the system is further improved. This enhanced configuration not only promotes more complete consumption of WP generation, but also minimizes electricity procurement during expensive periods, ultimately achieving the lowest operating cost and carbon emission levels among the three scenarios. Overall, the comparison demonstrates that the combined strategy of temperature flexibility, waste heat recovery, and optimized energy storage scheduling provides an effective pathway for maximizing WP utilization while simultaneously reducing economic and environmental costs.

Table 5 presents the operating cost, carbon emissions, and renewable energy consumption rate of IBs under the three scenarios.

Table 5. Comparison of Data Across the Three Scenarios.

Scenario	Carbon Emissions (kg)	Operating Costs (¥)	RE Consumption Rate
1	9600	128,000	78.2%
2	8100	105,000	88.7%
3	6812	89,000	100%

In Scenario 1, the system includes wind turbines, photovoltaic units, and an energy storage system (ESS), while the air conditioning temperature is fixed at 22 °C, without adjustable thermal load flexibility. The results show that the daily operating cost reaches CNY 128,000, carbon emissions amount to 9600 kg, and the renewable energy (RE) utilization rate is only 78.2%. Owing to the rigid HVAC operating mode, the system cannot effectively respond to electricity price variations, which results in considerable grid electricity purchases during peak-price periods (e.g., 18:00–20:00) and pronounced wind-photovoltaic (WP) curtailment around midday and during several nighttime intervals. This operating pattern not only leads to underutilization of renewable resources, but also increases the cost

of electricity procurement during expensive hours, making Scenario 1 the least favorable case in terms of both economic and environmental performance.

In Scenario 2, the fixed-temperature setting used in Scenario 1 is replaced by a temperature regulation strategy that permits indoor temperature variation within the comfort range of 20–24 °C. This modification increases the scheduling flexibility of the HVAC system and improves its ability to perform peak shaving. Under this scenario, the daily operating cost falls to CNY 105,000, carbon emissions decline to 8100 kg, and the renewable energy (RE) utilization rate rises to 88.7%. Relative to Scenario 1, these results correspond to reductions of 17.97% in operating cost and 15.63% in carbon emissions, together with an increase of 10.5 percentage points in RE utilization. From the operational viewpoint, the system is able to carry out pre-cooling and charge the ESS during low-price periods, thereby storing both thermal and electrical flexibility in advance. During high-price periods, the HVAC electricity demand is correspondingly reduced, while the ESS increases its discharge to support the load. Through this coordinated scheduling strategy, grid electricity purchase during peak hours is effectively suppressed, and the mismatch between renewable generation and load demand is alleviated. Consequently, the system not only reduces its dependence on the external grid, but also mitigates renewable energy curtailment and improves overall operational efficiency.

In Scenario 3, waste heat recovery is introduced as an additional source of cooling support after incorporating the temperature regulation strategy in Scenario 2. Through the reuse of recoverable thermal energy, part of the cooling demand is no longer supplied by the HVAC system, and the corresponding electricity consumption is therefore reduced. Under this condition, renewable generation together with the ESS, especially during expensive electricity periods, which further improves the overall operating status of the system. Quantitatively, the daily operating cost drops to CNY 89,000, carbon emissions fall to 6812 kg, and the renewable energy utilization rate reaches 100%, meaning that all available wind and photovoltaic power can be consumed locally. Compared with Scenario 2, the operating cost and carbon emissions are further reduced by 15.24% and 15.90%, respectively. These results confirm that Scenario 3 provides the most favorable overall outcome among the three cases from both economic and environmental perspectives.

Overall, the results demonstrate that the deployment of ESS improves peak-valley shifting capability, enhances renewable energy utilization, and lowers operating costs. Introducing temperature-controlled load flexibility further strengthens the coordination between load demand and ESS operation, thereby reducing grid electricity purchases during high-price periods. With the additional integration of WHR, renewable energy can be utilized more completely, enabling the system to simultaneously achieve the lowest operating cost, the lowest carbon emissions, and full consumption of WP generation.

The computational efficiency metrics of the C&CG framework are summarized as follows. Setting the termination tolerance $\epsilon = 10^{-4}$, convergence is reached rapidly within 4 main iterations. Using IBM ILOG CPLEX Optimization Studio 22.1.1 (IBM Corp., Armonk, NY, USA), the total execution runtime was 14.2 s, verifying its suitability for real-time engineering applications.

To cleanly isolate the independent contribution of waste heat recovery loops, a newly added Scenario 1b (Fixed Temp at 22 °C + WHR active) demonstrates an operational cost of CNY 112,000 and carbon emissions of 8400 kg. This explicitly proves that while WHR provides standalone economic benefits, combining it with temperature flexibility (Scenario 3) unlocks synergistic performance gains.

5.3. Sensitivity Analysis

To verify the robustness of the proposed optimization strategy against parameter uncertainties, a sensitivity analysis was performed on two critical factors: the efficiency of the waste heat recovery (WHR) system and the flexibility of the indoor temperature bounds. The sensitivity analysis results are summarized in Table 6.

Table 6. Sensitivity Analysis Results (Cost and Carbon Emissions).

Parameter Variation	Operating Cost (CNY)	Variation vs. Base	Carbon Emissions (kg)
Base Case (Scenario 3)	89,000	-	6812
Low Efficiency (−20%)	91,200	+2.47%	7050
High Efficiency (+20%)	87,100	−2.13%	6620
Tighter (21–23 °C)	94,960	+6.70%	7280
Wider (19–25 °C)	85,260	−4.20%	6490
IDM Parameter s = 1	86,400	-	6580
IDM Parameter s = 4	92,150	-	7120
Forecast Errors Expanded (+15%)	90,800	-	6990
HVAC COP Degraded (−10%)	93,400	-	7180

The performance of the WHR unit depends on its operating conditions. To evaluate this effect, the recovery efficiencies (ξ_{gas} and ξ_{water}) were varied by ±10% and ±20% relative to the base case (Scenario 3). As reported in Table 6, higher recovery efficiency unsurprisingly results in greater reductions in both operating cost and carbon emissions. More importantly, even when the efficiency decreases by 20%, the proposed strategy still maintains a clear advantage over the non-WHR case (Scenario 2). This result demonstrates that the proposed method remains economically effective even under conservative efficiency assumptions.

The allowable indoor temperature range determines the capacity of the building's virtual energy storage. We compared the base range (20–24 °C) with a tighter range (21–23 °C) and a wider range (19–25 °C). The analysis indicates that narrowing the comfort band reduces the flexibility of load shifting, leading to a 6.7% increase in operating costs. Conversely, widening the band by just 1 °C further reduces costs by 4.2%. This highlights the trade-off between user comfort and operational economy, validating that the selected range of 20–24 °C serves as a balanced and realistic baseline for intelligent buildings.

6. Conclusions

This paper presents a two-stage distributionally robust optimization method that combines virtual energy storage with waste heat recovery. The main conclusions are summarized as follows:

(1) A two-stage distributionally robust optimization model is established by jointly incorporating the flexibility of temperature-controlled loads and the utilization of waste heat recovery. Through coordinated control of air conditioning operation, the proposed method enables intelligent buildings to achieve economical and low-carbon operation without sacrificing indoor thermal comfort. In Scenario 3, the daily operating cost is reduced to CNY 89,000 and carbon emissions are lowered to 6812 kg, representing decreases of 30.47% and 29.06%, respectively, compared with Scenario 1. At the same time, the renewable energy utilization rate reaches 100%.

(2) To manage uncertainties caused by load disturbances and changing outdoor temperature conditions, the proposed two-stage distributionally robust optimization

framework introduces both building thermal inertia and adjustable uncertainty parameters, thereby enabling flexible control over the conservatism of the model. Under this framework, Scenario 2 achieves a 17.97% decrease in daily operating cost and a 15.63% reduction in carbon emissions compared with Scenario 1, while the renewable energy utilization rate is improved by 10.5 percentage points. These results confirm that the proposed method can effectively enhance both economic performance and environmental benefits.

(3) From the perspective of computational implementation, the proposed two-stage distributionally robust optimization problem can be solved efficiently using the column-and-constraint generation (C&CG) algorithm, which improves the tractability of the model. This method substantially improves solution efficiency while ensuring global convergence. The optimized scheduling strategy obtained in Scenario 3 enables the full local utilization of wind-photovoltaic (WP) energy. In addition, the results under multiple scenarios indicate that the proposed strategy exhibits strong robustness and good adaptability in systems with renewable energy integration.

Although the proposed method shows clear advantages, several limitations still deserve further study. First, to maintain computational tractability in the robust optimization process, the thermal dynamics of the building are represented by a simplified RC network with linearized constraints. While this formulation is adequate for control-oriented analysis, it may not fully capture the nonlinear thermal behavior of building materials under extreme weather conditions. Second, the current framework is established for a single intelligent building zone and does not explicitly account for power flow constraints or interaction mechanisms within larger building clusters or microgrid-based communities.

Future work will therefore focus on extending the proposed framework in two directions. On the one hand, higher-fidelity nonlinear thermal models and real-time predictive control methods will be incorporated to improve modeling accuracy and operational performance. On the other hand, the framework will be expanded to building clusters and community-scale energy systems in order to investigate inter-building energy interactions. In addition, dynamic market mechanisms, such as carbon trading and peer-to-peer energy sharing, will be introduced to further enhance the practical applicability of the proposed model.

Author Contributions: Conceptualization, H.Y., Y.L. and S.Z.; Methodology, H.Y., Y.L. and S.Z.; Validation, H.Y., Y.L. and S.Z.; Investigation, H.Y. and Y.L.; Resources, H.Y. and S.Z.; Writing—original draft, H.Y. and Y.L.; Writing—review and editing, H.Y., Y.L. and S.Z.; Supervision, H.Y.; Project administration, H.Y.; Funding acquisition, H.Y. All authors have read and agreed to the published version of the manuscript.

Funding: This work was supported by the Scientific Research Project of Characteristic Laboratories in Colleges and Universities in Shandong Province: Green and Low-carbon Smart Heating and Cooling Technology Characteristic Laboratory (PT2022TS01).

Data Availability Statement: The original contributions presented in this study are included in the article; further inquiries can be directed to the corresponding author.

Conflicts of Interest: The authors declare that the research was conducted in the absence of any commercial or financial relationships that could be construed as a potential conflict of interest.

References

1. Li, Z.; Lin, B.; Zheng, S.; Liu, Y.; Wang, Z.; Dai, J. A review of operational energy consumption calculation method for urban buildings. *Build. Simul.* **2020**, *13*, 739–751. [CrossRef]
2. Lv, Q. Intelligent building design based on green and low-carbon concept. *Energy Inform.* **2025**, *8*, 55. [CrossRef]

3. Allouhi, A.; El Fouih, Y.; Kousksou, T.; Jamil, A.; Zeraouli, Y.; Mourad, Y. Energy consumption and efficiency in buildings: Current status and future trends. *J. Clean. Prod.* **2015**, *109*, 118–130. [CrossRef]
4. Santamouris, M.; Vasilakopoulou, K. Present and future energy consumption of buildings: Challenges and opportunities towards decarbonisation. *e-Prime Adv. Electr. Eng. Electron. Energy* **2021**, *1*, 100002. [CrossRef]
5. Liu, J.; Zhai, Z.; Zhang, Y.; Wang, Y.; Ding, Y. Comparison of energy consumption prediction models for air conditioning at different time scales for large public buildings. *J. Build. Eng.* **2024**, *96*, 110423. [CrossRef]
6. Soret, G.M.; Vacca, P.; Tignard, J.; Hidalgo, J.P.; Maluk, C.; Aitchison, M.; Torero, J.L. Thermal inertia as an integrative parameter for building performance. *J. Build. Eng.* **2021**, *33*, 101623. [CrossRef]
7. Jeong, S.G.; Lee, J.; Chang, S.J.; Kim, S. Thermal and structural behavior of thermal inertia-reinforced mortars for building envelope applications. *Constr. Build. Mater.* **2023**, *384*, 131452. [CrossRef]
8. Ren, Z.; Gao, X.; Xiao, Y.; Liu, Y. Thermal comfort and energy conservation of a four-sided enclosed local heating device in a cold environment. *Build. Environ.* **2023**, *228*, 109837. [CrossRef]
9. Burnete, N.V.; Mariasiu, F.; Depcik, C.; Barabas, I.; Moldovanu, D. Review of thermoelectric generation for internal combustion engine waste heat recovery. *Prog. Energy Combust. Sci.* **2022**, *91*, 101009. [CrossRef]
10. Omara, A.A.M. Phase change materials for waste heat recovery in internal combustion engines: A review. *J. Energy Storage* **2021**, *44*, 103421. [CrossRef]
11. Nikkhah, S.; Allahham, A.; Royapoor, M.; Bialek, J.W.; Giaouris, D. Optimising building-to-building and building-for-grid services under uncertainty: A robust rolling horizon approach. *IEEE Trans. Smart Grid* **2021**, *13*, 1453–1467. [CrossRef]
12. Li, H.; Liu, T.; Chan, H.K.H.; Lu, H. Spatial data analysis for intelligent buildings: Awareness of context and data uncertainty. *Front. Big Data* **2022**, *5*, 1049198. [CrossRef]
13. Fang, F.; Yu, S.; Xin, X. Data-driven-based stochastic robust optimization for a virtual power plant with multiple uncertainties. *IEEE Trans. Power Syst.* **2021**, *37*, 456–466. [CrossRef]
14. Ibrahim, M.M.; Hasanien, H.M.; Farag, H.E.Z.; Omran, W.A. Energy management of multi-area islanded hybrid microgrids: A stochastic approach. *IEEE Access* **2023**, *11*, 101409–101424. [CrossRef]
15. Ma, M.; Long, Z.; Liu, X.; Lee, K.Y. Distributionally robust optimization of electric–thermal–hydrogen integrated energy system considering source–load uncertainty. *Energy* **2025**, *316*, 134568.
16. Li, Z.; Sun, H.; Xue, Y.; Li, Z.; Jin, X.; Wang, P. Resilience-Oriented Asynchronous Decentralized Restoration Considering Building and E-Bus Coresponse in Electricity-Transportation Networks. *IEEE Trans. Transp. Electrif.* **2025**, *11*, 11701–11713. [CrossRef]
17. Du, Y.; Xue, Y.; Wu, W.; Shahidehpour, M.; Shen, X.; Wang, B.; Sun, H. Coordinated Planning of Integrated Electric and Heating System Considering the Optimal Reconfiguration of District Heating Network. *IEEE Trans. Power Syst.* **2024**, *39*, 794–808. [CrossRef]
18. Wang, K.; Xue, Y.; Guo, Q.; Shahidehpour, M.; Zhou, Q.; Wang, B.; Sun, H. A Coordinated Reconfiguration Strategy for Multi-Stage Resilience Enhancement in Integrated Power Distribution and Heating Networks. *IEEE Trans. Smart Grid.* **2023**, *14*, 2709–2722. [CrossRef]
19. Chang, L.; Li, Z.; Tian, X.; Su, J.; Chang, X.; Xue, Y.; Li, Z.; Jin, X.; Wang, P.; Sun, H. A two-stage distributionally robust low-carbon operation method for antarctic unmanned observation station integrating virtual energy storage and hydrogen waste heat recovery. *Appl. Energy* **2025**, *400*, 126578. [CrossRef]
20. Lu, X.; Zhou, K. A distributionally robust optimization approach for optimal load dispatch of energy hub considering multiple energy storage units and demand response programs. *J. Energy Storage* **2024**, *78*, 110085. [CrossRef]
21. Zhang, Q.; Mu, Y.; Jia, H.; Yu, X.; Hou, K. Distributionally robust optimization configuration method for island microgrid considering extreme scenarios. *Energy AI* **2024**, *17*, 100389. [CrossRef]
22. Zhang, Z.; Yang, S.; Ma, Y.; Sun, S.; Yu, P.; Yang, F. Constrained distributionally robust optimization for day-ahead dispatch of rural integrated energy systems with source and load uncertainties. *Front. Energy Res.* **2024**, *12*, 1411152. [CrossRef]
23. Rodríguez Jara, E.Á.; Sánchez De La Flor, F.J.; Álvarez Domínguez, S.; Molina Félix, J.L.; Salmerón Lissén, J.M. A new analytical approach for simplified thermal modelling of buildings: Self-adjusting RC-network model. *Energy Build.* **2016**, *130*, 85–97. [CrossRef]
24. Qi, J.; Guo, J.; Zhang, Y. An IDM-based two-stage robust balance analysis model for high-proportion renewable energy integration through HVDC system. In Proceedings of the 2023 8th International Conference on Power and Renewable Energy (ICPRE), Shanghai, China, 22–25 September 2023; pp. 1619–1626.
25. Liu, Y.; Chen, X.; Wu, L.; Ye, Y. An IDM-based distributionally robust economic dispatch model for integrated electricity-heat-gas microgrid considering wind power. *CSEE J. Power Energy Syst.* **2022**, *9*, 1182–1192.
26. Fan, G.; Peng, C.; Wang, X.; Wu, P.; Yang, Y.; Sun, H. Optimal scheduling of integrated energy system considering renewable energy uncertainties based on distributionally robust adaptive MPC. *Renew. Energy* **2024**, *226*, 120457. [CrossRef]
27. Wu, S.; Li, Q.; Liu, J.; Zhou, Q.; Wang, C. Bi-level optimal configuration for combined cooling heating and power multi-microgrids based on energy storage station service. *Power Syst. Technol.* **2021**, *45*, 3822–3829.

28. *ANSI/ASHRAE Standard 55-2020*; Thermal Environmental Conditions for Human Occupancy. American Society of Heating, Refrigerating and Air-Conditioning Engineers: Atlanta, Georgia, 2020.
29. *GB 50736-2012*; Design Code for Heating Ventilation and Air Conditioning of Civil Buildings. China Architecture & Building Press: Beijing, China, 2012.

Disclaimer/Publisher's Note: The statements, opinions and data contained in all publications are solely those of the individual author(s) and contributor(s) and not of MDPI and/or the editor(s). MDPI and/or the editor(s) disclaim responsibility for any injury to people or property resulting from any ideas, methods, instructions or products referred to in the content.